CRYSTAL GROWTH & DESIGN

Article

pubs.acs.org/crystal

Three-Dimensional Extended Frameworks Constructed from Dinuclear Lanthanide(III) 1,4-Naphthalenedicarboxylate Units with Bis(2,2′-biimidazole) Templates: Syntheses, Structures, and Magnetic and Luminescent Properties

Ying-Bing Lu,*[,†] Fang-Mei Jian,[†] Shuang Jin,[†] Jun-Wei Zhao,*[,‡] Yong-Rong Xie,[†] and Guo-Tian Luo[†]

[†]Jiangxi Key Laboratory of Function of Materials Chemistry, College of Chemistry and Chemical Engineering, Gannan Normal University, Ganzhou, 341000, People's Republic of China

[‡]Henan Key Laboratory of Polyoxometalate Chemistry, College of Chemistry and Chemical Engineering, Henan University, Kaifeng, Henan 475004, People's Republic of China

Supporting Information

ABSTRACT: Eight unprecedented Ln-NDC coordination polymers with BBI as templates {[HBBI][Ln(NDC)$_2$(H$_2$O)]·H$_2$O [Ln = La (**1**), Pr (**2**)], [HBBI]$_2$[Sm(NDC)$_2$(H$_2$O)]$_2$·1/2H$_2$O (**3**), and [HBBI][Ln(NDC)$_2$(H$_2$O)] [Ln = Eu (**4**), Gd (**5**), Tb (**6**), Dy (**7**), Er (**8**)] [Ln = lanthanide, H$_2$NDC = 1,4-naphthalenedicarboxylic acid, BBI = bis(2,2′-biimidazole)]} have been hydrothermally synthesized and structurally characterized by elemental analyses, IR spectra, and single-crystal X-ray diffraction. Complexes **1**−**8** crystallize in the monoclinic space group $P2_1/c$ and display similar (8,8)-connected 3-D frameworks with different dinuclear Ln secondary building units due to the effect of Ln contraction and diverse coordination modes of NDC^{2-} ligands. As the ionic radii of Ln ions decrease, the coordination numbers of Ln ions decrease from 10, to 9, to 8. The variable-temperature magnetic properties of **2**−**8** have been investigated. The strong fluorescent emissions of **4** demonstrate that ligand-to-Eu^{III} energy transfer is efficient. In addition, thermogravimetric analyses and optical diffuse reflectance spectra of these compounds are also described.

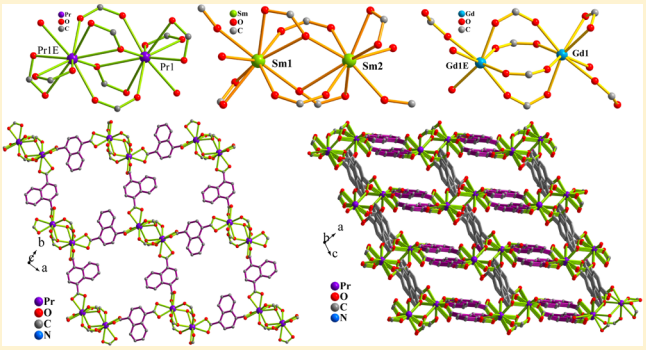

INTRODUCTION

The rational design and construction of metal−organic frameworks (MOFs) based upon assembly of metal ions and organic ligands are currently of great interest, which not only stems from their exciting structural architectures, but also from their potential applications in the fields of sorption, catalysis, magnetism, and photochemistry.[1] To date, many of the efforts have so far been devoted to the study of transition-metal-based MOFs. The lanthanide (Ln) analogues are also highly sought after because Ln ions possess high coordination numbers, flexible coordination geometries, and the effect of Ln contraction that can afford structural diversity.[2] Moreover, Ln-based compounds can show distinct characteristic luminescent emissions and large anisotropic magnetic moments arising from a large number of spins and strong spin−orbit coupling, which are much different from those of transition-metal compounds.[3] In addition, aromatic carboxylate coordination complexes have been extensively investigated in past decades due to their strong coordination capability, their large conjugated systems, and the possibility of offering new functional materials.[4] The 1,4-naphthalenedicarboxylic acid (H$_2$NDC) ligand as an important aromatic carboxylic ligand has shown an excellent bridging role in constructing novel MOFs with interesting optical[5] and magnetic[6] properties as well as gas storage ability[7] because of its various coordinating modes (Table 1), high symmetry, and structural rigidity.[8] However, up to now much more research on the coordination chemistry of the H$_2$NDC ligand has been focused on transition-metal-based MOFs,[9] and investigations on NDC-bridged Ln MOFs are very rare. For example, in 2004, Gao's group reported two three-dimensional (3-D) MOFs, [Ln$_7$(μ_3-OH)$_8$(NDC)$_6$(OH)$_{0.5}$(CH$_3$COO)$_{0.5}$(H$_2$O)$_7$]·4H$_2$O, constructed from unprecedented heptanuclear [Ln$_7$(μ_3-OH)$_8$]$^{13+}$ (Ln = Ho, Yb) cluster units.[10] In 2005, several Ln-NDC MOFs with 4,4′-bpy and phen as coligands, [Ln$_2$(NDC)$_3$(H$_2$O)$_2$]·H$_2$O (Ln = Eu, Gd), [Ln$_2$(NDC)$_3$(4,4′-bpy)$_{0.5}$(H$_2$O)$_3$]·(4,4′-bpy) (Ln = Eu, Yb; 4,4′-bpy = 4,4′-bipyridine),[11a] and [Ln$_2$(NDC)$_3$(phen)$_2$(H$_2$O)$_2$] (Ln = La, Eu, Ho; phen = 1,10-phenanthroline),[11b] were isolated by Jin's group. Later, Chen's group obtained [Eu(1,4-NDA)$_{1.5}$(DMF)$_2$], [Nd$_2$(1,4-

Received: December 7, 2013
Revised: February 18, 2014
Published: February 28, 2014

Table 1. Various Coordination Modes for the H_2NDC Ligand

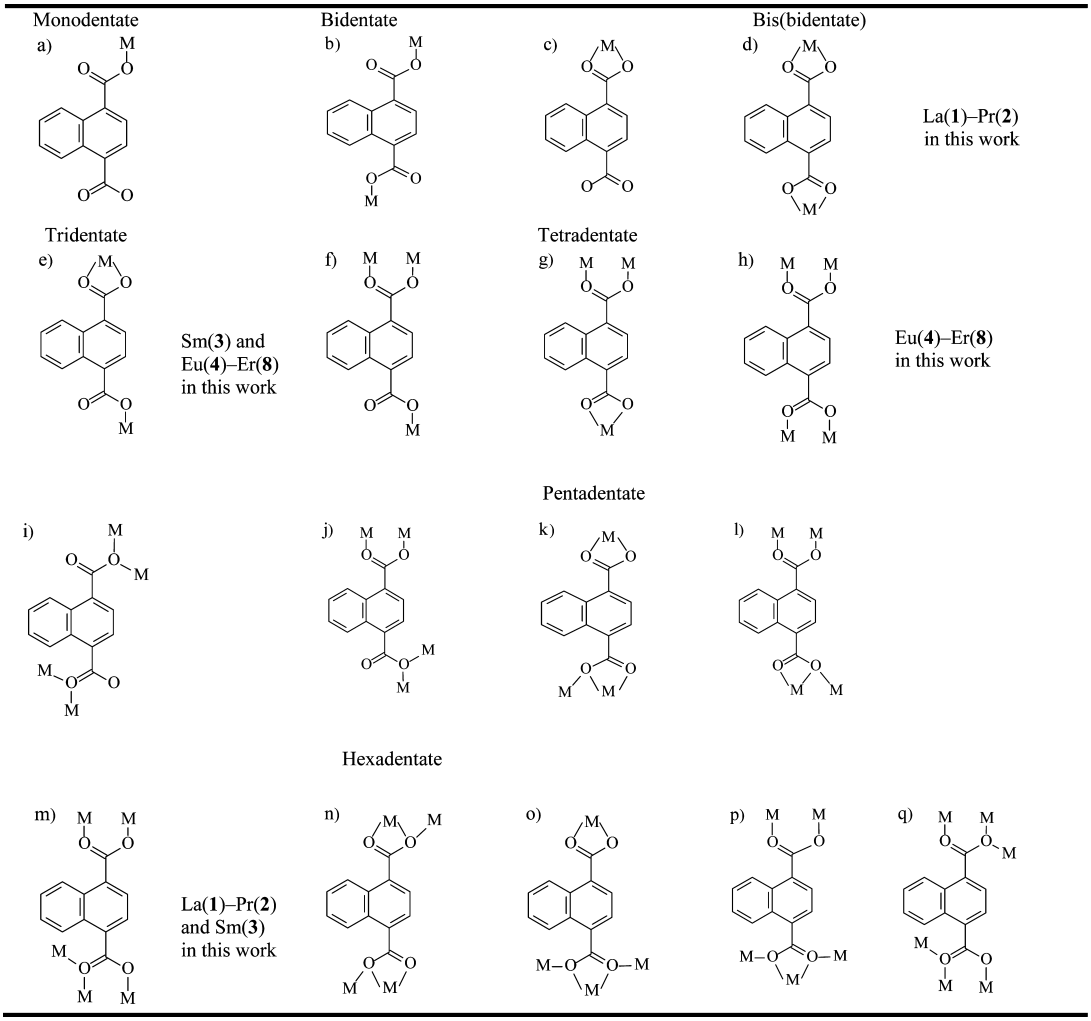

$NDA)_3(DMF)_4]\cdot H_2O$, and $[La_2(1,4\text{-}NDA)_3(DMF)_4]\cdot 0.5H_2O$[12] and Zhang's group obtained $[Y_2(NDC)_3(e\text{-urea})_4]\cdot$ e-urea [e-urea = ethyleneurea][13] by solvothermal reaction in dimethylformamide (DMF) and ethyleneurea, respectively.

On the other hand, besides the bridging ligands, many other components such as coligands or template agents also play a crucial role in the formation of MOF materials; therefore, the employment of coligands or template agents in fabricating MOFs has attracted growing interest in recent years.[14] In general, on the basis of previous reports, the coligands coordinate to metal centers as ancillary ligands while the template agents (being neutral or charged) do not coordinate to metal centers but occupy specific space and interact with other components via weak interactions in the resulting structures. Especially for some coligands, for instance, polydentate N-donor ligands are facile to protonate and can act as templates to guide the formation of anionic MOFs with special structures.[15] In the past decade, the bis(imidazole) ligands as an important family of polydentate N- donor ligands have attracted much attention and have been usually used as coligands or template agents in the formation of MOFs with unique structure types and associated properties.[16] However, to the best of our knowledge, lanthanide MOFs of a polycarboxylate containing 2,2′-biimidazole (BBI) components have not yet been reported. We decided to construct Ln-based MOFs with mixed BBI and H_2NDC components by a hydrothermal technique based on the following considerations: (1) the rigid H_2NDC ligand contains two carboxylate groups, promising rich and versatile coordination modes to achieve diverse structures with interesting topology; (2) the BBI ligand based lanthanide complexes remain largely unexplored, which offers us a good opportunity to exploit this domain with the aim of discovering novel Ln complexes with N-donor ligand; (3) aromatic H_2NDC and BBI ligands, possessing electron-conjugate systems, may be good chromophores and act as magnetic mediators and/or luminescent sensitizers via the "antenna effect" in the Ln-based complexes. Under the guidance of these considerations, eight novel Ln-NDC-based extended MOFs with protonated BBI as templates have been synthesized and characterized: $[HBBI]_2[Ln(NDC)_2(H_2O)]_2\cdot 2H_2O$ [Ln = La (**1**), Pr (**2**)]; $[HBBI]_2[Sm(NDC)_2(H_2O)]_2\cdot 1/2H_2O$ (**3**); $[HBBI]_2[Ln(NDC)_2(H_2O)]_2$ [Ln = Eu (**4**), Gd (**5**), Tb (**6**), Dy (**7**), Er (**8**)] [Ln = lanthanide, H_2NDC = 1,4-naphthalenedicarboxylic acid, BBI = bis(2,2′-biimidazole)]. Their common features show similar (8,8)-connected 3-D frameworks while they are constructed by different dinuclear Ln secondary building units (SBUs) arising from the effect of Ln contraction and diverse coordination modes of NDC^{2-} ligands. The magnetic behaviors of **2**–**8** have been studied. The luminescence properties of the Eu^{III} compound have also been investigated in detail.

dx.doi.org/10.1021/cg401825f | *Cryst. Growth Des.* 2014, 14, 1684–1694

Table 2. X-ray Diffraction Crystallographic Data for 1−4

	1	2	3	4
formula	$C_{30}H_{23}LaN_4O_{10}$	$C_{30}H_{23}N_4O_{10}Pr$	$C_{60}H_{43}N_8O_{18.5}Sm_2$	$C_{30}H_{21}Eu\ N_4O_9$
fw	738.43	740.44	1472.72	733.47
temp (K)	296(2)	296(2)	293(2)	296(2)
crystal system	monoclinic	monoclinic	monoclinic	monoclinic
space group	$P2_1/c$	$P2_1/c$	$P2_1/c$	$P2_1/c$
a (Å)	11.15780(10)	11.179(5)	23.0803(7)	11.72250(10)
b (Å)	15.5651(2)	15.482(7)	15.5854(3)	15.74660(10)
c (Å)	16.1486(2)	16.052(7)	15.6694(4)	15.42610(10)
β (deg)	103.75	103.943(4)	103.898(2)	104.63
V (Å^3)	2724.18(5)	2696(2)	5471.5(2)	2755.18(3)
Z	4	4	4	4
D_c (g/cm^3)	1.800	1.877	1.788	1.768
μ (mm^{-1})	1.639	1.843	2.213	2.342
F(000)	1472	1508	2924	1456
no. reflns collected	33 192	16 045	37 629	19 570
independent reflns	4788	4797	9841	5103
R_{int}	0.0193	0.0184	0.0240	0.0230
θ range (deg)	2.29−25.00	2.61−25.35	2.73−25.25	1.80−25.50
params/restraints/data	4788/6/418	4797/6/418	9841/21/820	5103/3/403
R_1 [$I > 2\sigma(I)$]	0.0165	0.0323	0.0332	0.0254
wR_2 (all data)	0.0624	0.1174	0.1155	0.0759
GOF on F^2	1.013	1.013	0.986	1.012
ρ_{max}/ρ_{min} (e Å^{-3})	0.522/−0.405	0.837/−0.959	1.957/−1.241	1.303/−0.474

Table 3. X-ray Diffraction Crystallographic Data for 5−8

	5	6	7	8
formula	$C_{30}H_{21}GdN_4O_9$	$C_{30}H_{21}N_4O_9Tb$	$C_{30}H_{21}DyN_4O_9$	$C_{30}H_{21}ErN_4O_9$
fw	738.76	740.43	744.01	748.77
temp (K)	293(2)	296(2)	296(2)	296(2)
crystal system	monoclinic	monoclinic	monoclinic	monoclinic
space group	$P2_1/c$	$P2_1/c$	$P2_1/c$	$P2_1/c$
a (Å)	11.7508(4)	11.74380(10)	11.74390(10)	11.7276(2)
b (Å)	15.7702(4)	15.74570(10)	15.7292(2)	15.6930(3)
c (Å)	15.3590(5)	15.30420(10)	15.2552(2)	15.2043(3)
β (deg)	104.7950	105.0510(10)	105.1690(10)	105.3080(10)
V (Å^3)	2751.85(15)	2732.88(3)	2719.79(5)	2698.94(9)
Z	4	4	4	4
D_c (g/cm^3)	1.783	1.800	1.817	1.843
μ (mm^{-1})	2.475	2.653	2.813	3.176
F(000)	1460	1464	1468	1476
no. reflns collected	21 612	21 860	19 021	18 725
independent reflns	6303	5096	5027	4954
R_{int}	0.0444	0.0387	0.0256	0.0370
θ range (deg)	2.83−27.49	1.80−25.50	1.89−25.50	1.90−25.50
params/restraints/data	6303/3/404	5096/3/403	5027/3/403	4954/3/403
R_1 [$I > 2\sigma(I)$]	0.0397	0.0236	0.0291	0.0394
wR_2 (all data)	0.1215	0.0569	0.0877	0.0859
GOF on F^2	0.978	1.004	1.018	0.965
ρ_{max}/ρ_{min} (e Å^{-3})	2.167/−2.050	0.517/−0.591	2.139/−1.019	4.713/−1.028

EXPERIMENTAL SECTION

Materials and Methods. All chemicals were used as purchased without further purification. Element analyses of C, H, and N were carried out with an Elementar Vario MICRO. The Fourier transform infrared (FT-IR) spectra were measured on a Nicolet Magna 750 FT-IR spectrophotometer in the region of 4000−400 cm^{-1} using KBr pellets. Magnetic susceptibilities were acquired by using a Quantum Design PPMS Model 6000 magnetometer. Optical diffuse reflectance spectra were measured with a PE Lambda 900 UV−vis−NIR spectrophotometer at room temperature. Initially, the 100% line flatness of the spectrophotometer was set using barium sulfate ($BaSO_4$). Thermogravimetric analysis (TGA) was performed on a Netzsch Sta449C thermoanalyzer under air atmosphere with a heating rate 10 °C/min. Photoluminescence analyses were measured on an Edinburgh FL S920 fluorescence spectrometer. Powder X-ray diffraction (PXRD) patterns were obtained from a Rigaku DMAX2500 powder diffractometer at 40 kV and 100 mA using Cu Kα (λ = 1.540 56 Å), with a scan speed of 0.375 s/step and a step size of 0.06°. The simulated powder patterns were calculated using single-crystal X-ray diffraction data and processed by the free Mercury v1.4 program provided by the Cambridge Crystallographic Data Centre.

dx.doi.org/10.1021/cg401825f | Cryst. Growth Des. 2014, 14, 1684−1694

Preparations of 1−8. A representative experiment precedure is described below: a mixture of $Ln(NO_3)_3{\cdot}nH_2O$ (0.5 mmol), H_2NDC (0.5 mmol), BBI (0.5 mmol), and water (10 mL) with the starting pH value of 6.0 was sealed into a 25-mL Teflon-lined stainless steel container under autogenous pressure, kept at 120 °C for 3 days, and then cooled to room temperature at a rate of 5 °C/h. Block single crystals suitable for X-ray analysis were obtained. Complexes **1**−**8** are air-stable and insoluble in water. Yield: 40% (based on La) for **1**; 35% (based on Pr) for **2**; 37% (based on Sm) for **3**; 25% (based on Eu) for **4**; 30% (based on Gd) for **5**; 20% (based on Tb) for **6**; 32% (based on Dy) for **7**; 23% (based on Er) for **8**. Anal. Calcd for **1**: C, 48.80; H, 3.14; N, 7.59. Found: C, 48.12; H, 3.35; N, 7.38. Anal. Calcd for **2**: C, 48.66; H, 3.13; N, 7.57. Found: C, 48.07; H, 3.51; N, 7.21. Anal. Calcd for **3**: C, 48.93; H, 2.94; N, 7.61. Found: C, 48.25; H, 3.35; N, 7.81. Anal. Calcd for **4**: C, 49.13; H, 2.89; N, 7.64. Found: C, 48.86; H, 3.29; N, 7.48. Anal. Calcd for **5**: C, 48.77; H, 2.87; N, 7.58. Found: C, 48.32; H,3.29; N, 7.69. Anal. Calcd for **6**: C, 48.43; H, 2.85; N, 7.53. Found: C, 48.02; H, 3.20; N, 2.57. Anal. Calcd for **7**: C, 48.66; H, 2.86; N, 7.57. Found: C, 48.19; H, 3.18; N, 7.49. Anal. Calcd for **8**: C, 48.12; H, 2.83; N, 7.48. Found: C, 47.85; H, 3.11; N,7.26. IR (KBr, cm^{-1}) for **1**: 3450m 3140w 1609s 1564s 1518s 1465m 1404vs 1359vs 1261m 1207m 1101m 1018w 950w 836m 783s 670w 556s 456m 442s; for **2**: 3430m 3150m 2782w 1616s 1569s 1528s 1466s 1405vs 1364vs 1262m 1214m 1091m 1023w 941w 832m 791s 682m 566m 477m; for **3**: 3412w 3132w 1624s 1549vs 1457s 1420vs 1374vs 1268m 1215m 1094m 821s 738s 662w 563m 473w; for **4**: 3526m 3344m 3140m 2769m 1639s 1533vs 1457s 1435vs 1359vs 1253m 1222m 1101m 829s 761vs 677w 563s 450m; for **5**: 3412w 3140w 1655s 1564vs 1465vs 1420vs 1374vs 1268m 1230m 1101m 1026w 980w 821m 753m 685w 579m 465m; for **6**: 3435s 3140w 1647s 1541s 1473s 1435s 1374s 1261m 1200m 1086m 1033w 927w 821m 761m 631m 556m 450m 405m; for **7**: 3428m 3147w 1647s 1564s 1473m 1435s 1374s 1268w 1200w 1109w 776m 670w 556m 427w; for **8**: 3435m 3147w 2821w 1655s 1556s 1473s 1427vs 1359vs 1276w 1215w 1101w 821m 761m 571m 442w 405w.

X-ray Crystallography. The intensity data collections for **1**−**8** were collected on a Rigaku Mercury CCD diffractometer equipped with graphite-monochromated Mo Kα radiation (λ = 0.710 73 Å) using an ω-scan technique at 293 K. Intensity data sets were reduced by the CrystalClear software.[17] The structures were solved by direct methods with the Siemens SHELXTL version 5 package of crystallographic software[18] and refined by full-matrix least-squares techniques. Non-hydrogen atoms were located by difference Fourier maps and subjected to anisotropic refinement. Hydrogen atoms attached to carbon and nitrogen atoms were geometrically placed. All hydrogen atoms were refined isotropically as a riding mode using the default SHELXTL parameters. Pertinent crystal data and structure refinement results for **1**−**8** are summarized in Tables 2 and 3, and selected bond lengths and bond angles are listed in Table S1 in the Supporting Information.

RESULTS AND DISCUSSION

Synthesis. Hydrothermal synthesis has recently been proven to be a useful technique in the preparation of MOF materials. Up to now, several Ln complexes with different organic templates have been synthesized and structurally characterized. Most of these complexes were synthesized under hydrothermal conditions.[19] In a specific hydrothermal process, many factors can affect the formation and crystal growth of products, such as the type of initial reactants, starting concentration, pH value, reaction time, and temperature. Complexes **1**−**8** were obtained by hydrothermal reactions of the corresponding $Ln(NO_3)_3$ with BBI and H_2NDC ligands. In our case, parallel experiments showed that the pH value and temperature of the reaction system are crucial for the crystallization of compounds. No suitable product is obtained at 100, 140, and 160 °C in similar reactions. Complexes **1**−**8** could only be obtained in the pH range 5.0−6.0 of the starting solution. At pH above 6.0, no crystalline phase was formed and the products are amorphous. This is because the N atom of the BBI ligand is favorable to be protonated under the acidic condition, which acts as template effect. In this paper, the template effects of protonated bis(2,2′-biimidazole) (BBI) components lie in thee aspects: (a) the formation of rich hydrogen bonds between protonated BBI ligands and NDC ligands can enhance the stability of structures of **1**−**8**; (b) in comparison with those reported Ln-based MOFs only linked by NDC ligands,[12,13] the 3-D templated architectures of **1**−**8** possess different size and shape channels, which indicate that the BBI components can influence the size and shape of channels; (c) protonated (BBI) components can function as countercations to balance the negative charge of the anionic backbones. Moreover, in the three isomorphous series, the powder X-ray diffraction patterns of Pr (**2**), Sm (**3**), and Tb (**6**) are in good agreement with the calculated patterns based on the single-crystal solution, indicating their good phase purity (Figure S1 in Supporting Information).

Structural Description. X-ray crystal structural analyses reveal that **1**−**8** crystallize in the monoclinic space group $P2_1/c$. Their common feature is that they adopt the organic−inorganic hybrid 3-D extended frameworks constructed from dinuclear Ln-NDC units with BBI templates. Due to the effect of Ln contraction and diverse coordination modes of NDC ligands, the structures of dinuclear Ln-NDC units are somewhat different (Scheme 1). On going from La to Er, the coordination

Scheme 1. Three Types of Dinuclear Ln-NDC Units (a) for 1 and 2, (b) for 3, and (c) for 4−8[a]

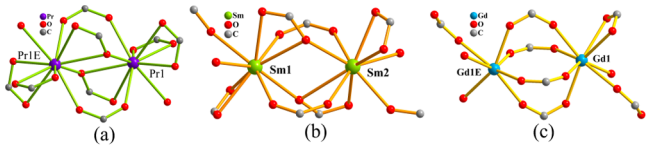

[a]E: 1 − x, −y, −z.

numbers of Ln ions decrease from 10, to 9, to 8 as the ionic radii of Ln ions decrease. X-ray diffraction structural analyses reveal that **1** and **2** are isomorphous and possess the 3-D architectures based on dinuclear Ln clusters (Ln = La^{3+}, Pr^{3+}) and NDC^{2-} connectors; hence only the structure of **2** will be representatively discussed in detail. As shown in Figure 1a, the asymmetric unit of **2** consists of one crystallographically unique Pr^{3+} cation, two crystallographically independent and fully deprotonated NDC^{2-} anions, one coordinated water molecule, one monoprotonated $[HBBI]^+$ cation, and one guest water molecule. The coordination environment around the $Pr1^{3+}$ cation can be clearly seen from Figure 1b. The $Pr1^{3+}$ cation is 10-coordinated by nine carboxylate oxygen atoms from six different NDC^{2-} ligands and one coordinated water molecule, forming a distorted trigonal hexadecahedron.

The Pr−O bond distances are in the range 2.489(2)−2.689(2) Å, which is comparable to those documented values in the previous literature.[20] In the asymmetric unit of **2**, one NDC^{2-} ligand coordinates to the $Pr1^{3+}$ cation via a carboxylic oxygen atom while the other NDC^{2-} ligand links to the $Pr1^{3+}$ cation through two carboxylic oxygen atoms. Two adjacent asymmetric units are combined together by four NDC^{2-} ligands giving rise to the dinuclear Ln-NDC molecular units (Figure 1c), in which two NDC^{2-} ligands employ the bidentate bridging role and two NDC^{2-} ligands utilize the tridentate

dx.doi.org/10.1021/cg401825f | Cryst. Growth Des. 2014, 14, 1684−1694

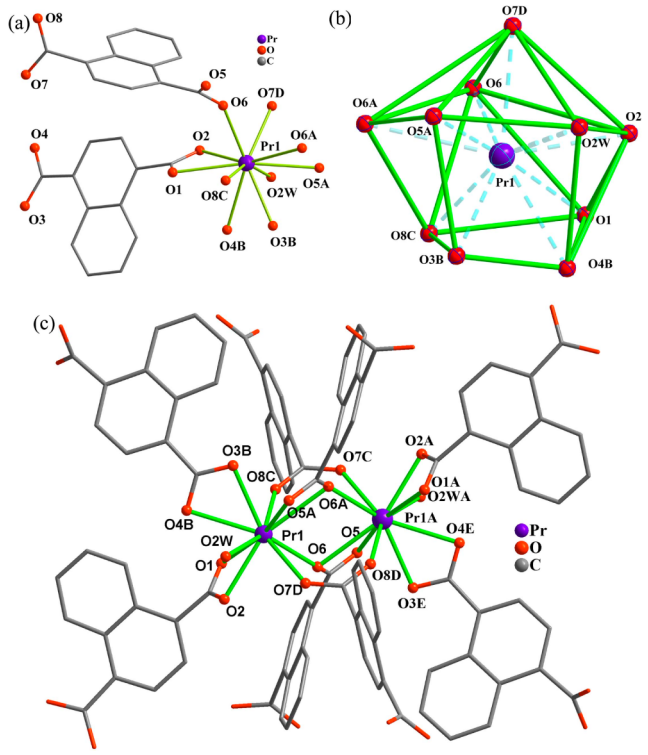

Figure 1. (a) Asymmetric molecular unit of **2** with the selected numbering scheme. The monoprotonated $[HBBI]^+$ cation and lattice water molecule are omitted for clarity. (b) Coordination polyhedron around the $Pr1^{3+}$ ion in **2**. (c) Dimeric molecular unit of **2**. Symmetric code: A: $1-x, -y, -z$; B: $-x, 0.5+y, -0.5-z$; C: $1-x, 0.5+y, -0.5-z$; D: $x, -0.5-y, 0.5+z$; E: $1+x, -0.5-y, 0.5+z$.

bridging role. The distance of two $Pr1^{3+}$ cations is 4.026 Å. Although the NDC^{2-} ligand has more than 17 coordination modes, the NDC^{2-} ligands in **2** adopt only the μ_4-η^1:η^1:η^1:η^1 and μ_5-η^1:η^1:η^1:η^2 bridging modes (Table 1). First, neighboring dinuclear Ln-NDC molecular units are bridged by the μ_4-η^1:η^1:η^1:η^1 bis-bidentate NDC^{2-} ligands to generate the infinite 2-D sheet architecture (Figure 2). Second, adjacent sheets can be further connected through μ_5-η^1:η^1:η^1:η^2 pentadentate NDC^{2-} ligands forming the 3-D framework with 1-D squarer channels along the *b* direction (Figure 2b). The monoprotonated $[HBBI]^+$ cations and guest water molecules occupy the void interspace region and interact with the carboxylic oxygen atoms and coordinated water molecules of frameworks through hydrogen bonds with O−H···O distances of 2.780(4)−3.024(4) Å and N−H···O distance of 2.758(4) Å (Figure S2, Table S2 in the Supporting Information).

In addition, it has proven that the network topological approach is a crucial and essential tool for analyzing the structures of MOFs.[21] By reducing complicated MOFs to simple node-and-connector reference nets, the topological approach has been widely used in the analyses of structures in recent years.[20,22] A better insight into the nature of the intricate 3-D framework of **2** can be achieved by making use of the topological approach. In the framework of **2**, the dinuclear Ln-NDC molecular units can be viewed as eight-connected nodes and the NDC^{2-} ligands act as connectors; thus, the 3-D framework can be reduced to an eight-connected net (Figure 2c). A topological analysis of this net was performed with OLEX.[23] The long topological (O'Keeffe) vertex symbol is $3{\cdot}4{\cdot}5_2{\cdot}4{\cdot}4{\cdot}3{\cdot}4{\cdot}3{\cdot}4{\cdot}5_2{\cdot}4{\cdot}4{\cdot}4{\cdot}4{\cdot}4{\cdot}6_6{\cdot}4{\cdot}3{\cdot}4{\cdot}5_2{\cdot}4{\cdot}3{\cdot}4{\cdot}4{\cdot}3{\cdot}4{\cdot}4$ and the short vertex (Schläfli) symbol is $3^6{\cdot}4^{18}{\cdot}5^3{\cdot}6^1$.

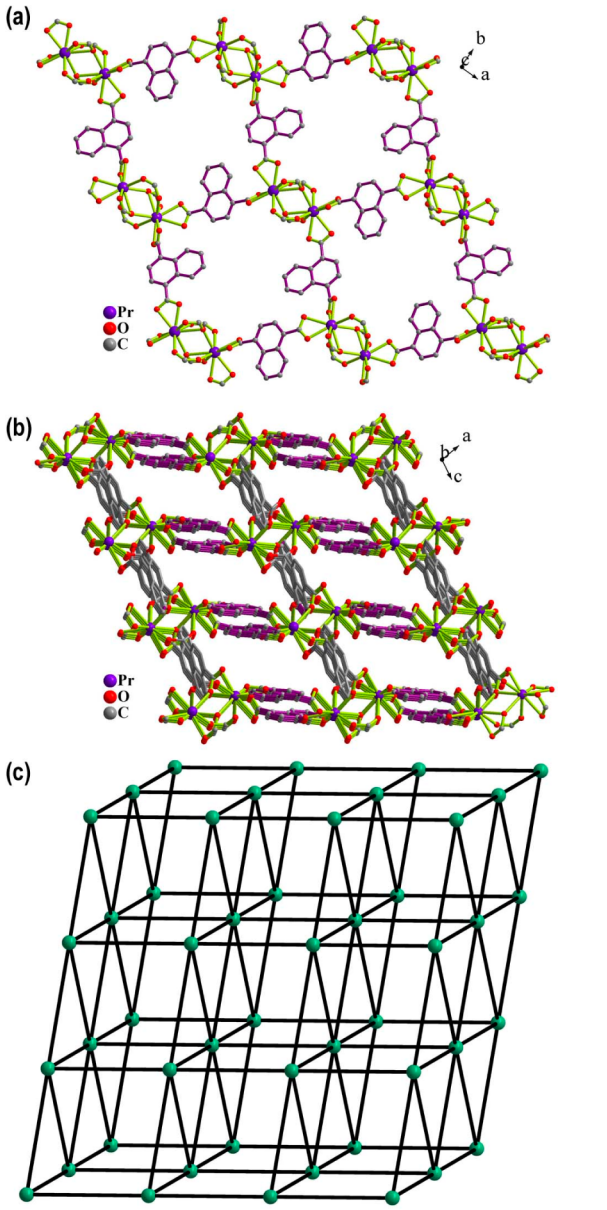

Figure 2. (a) The 2-D sheet constructed from dinuclear Ln-NDC molecular units by the μ_4-η^1:η^1:η^1:η^1 bis-bidentate NDC ligands. (b) The 3-D framework formed by 2-D sheets via the μ_5-η^1:η^1:η^1:η^2 pentadentate NDC ligands. (c) The 2-D topological network of **2**.

Athough the 3-D framework of **3** based on dinuclear Sm^{3+} clusters and NDC^{2-} connectors is very similar to those of **1** and **2**, the molecular construction of **3** is somewhat different from those of **1** and **2**. First, the dimeric unit of **3** contains two crystallographically unique Sm^{3+} cations ($Sm1^{3+}$ and $Sm2^{3+}$), four crystallographically unique deprotonated NDC^{2-} anions, two coordinated water molecules, two monoprotonated $[HBBI]^+$ cation, and one-half guest water molecule (Figure 3a). Second, two Sm^{3+} cations in **3** adopt the nine-coordinated trigonal tetradecahedron coordination geometries established by eight carboxylate oxygen atoms from six different NDC^{2-} ligands [Sm−O, 2.380(2)−2.827(2) Å] and one coordinated water molecule oxygen atom [Sm−O, 2.482(4)−2.468(3) Å] (Figure 3b,c). The distance between the $Sm1^{2+}$ and $Sm2^{2+}$

dx.doi.org/10.1021/cg401825f | *Cryst. Growth Des.* 2014, 14, 1684−1694

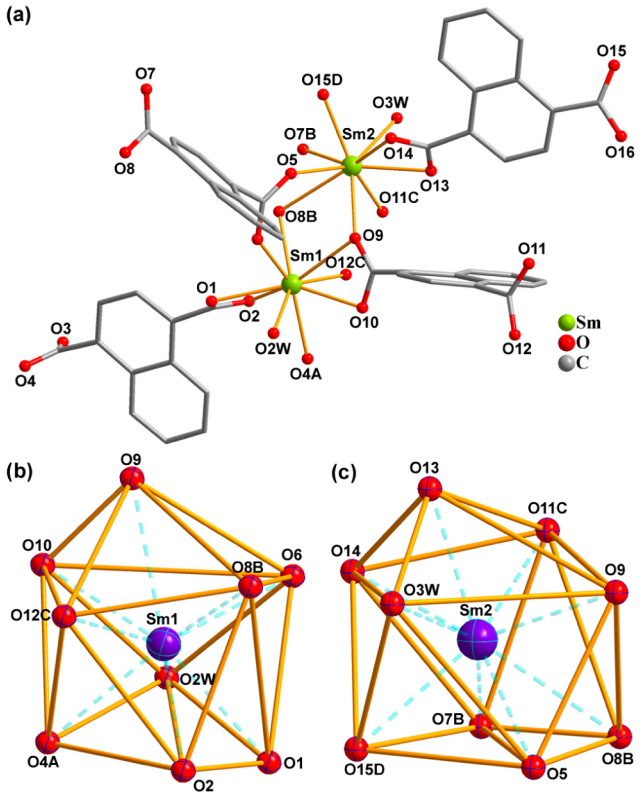

Figure 3. (a) Dimeric molecular unit of **3**. The monoprotonated $[HBBI]^+$ cation and lattice water molecule are omitted for clarity. (b) Coordination polyhedron around the $Sm1^{3+}$ ion in **3**. (c) Coordination polyhedron around the $Sm2^{3+}$ ion in 3. Symmetric code: A: $1-x, -0.5+y, 1.5-z$; B: $x, 2.5-y, 0.5+z$; C: $x, 1.5-y, 0.5+z$; D: $-x, 0.5+y, 0.5-z$.

cations is 4.035 Å. Third, in the construction of the 3-D framework of **3**, the NDC^{2-} ligands adopt the μ_3-η^1:η^1:η^1 and μ_5-η^1:η^1:η^1:η^2 bridging modes (Table 1). Specifically speaking, the creation of the infinite 2-D sheet architecture in the *ab* plane based on adjacent dimeric molecular units is through the μ_5-η^1:η^1:η^1:η^2-NDC^{2-} bridges (Figure S3a in the Supporting Information) while adjacent 2-D sheets are joined together via the μ_3-η^1:η^1:η^1-NDC^{2-} connectors forming the 3-D framework with 1-D squarer channels filled by monoprotonated $[HBBI]^+$ cations and guest water molecules (Figure S3b in the Supporting Information). It should be noted that the 3-D framework of **3** employs the same topological network to **1** and **2**.

Complexes **4**–**8** are isomorphous and also display the 3-D extended architectures constructed from dinuclear Ln clusters (Ln = Eu^{3+}, Gd^{3+}, Tb^{3+}, Dy^{3+}, Er^{3+}) by NDC^{2-} connectors, which are very similar to those of **1**–**3**. However, some evident differences can be observed: (a) The asymmetric units of **4**–**8** include one crystallographically independent Ln^{3+} cation, two crystallographically independent and fully deprotonated NDC^{2-} anions, one coordinated water molecule, and one monoprotonated $[HBBI]^+$ cation and two asymmetric units can also form the similar dinuclear Ln clusters to **1**–**3**, but there is no guest water molecule in **4**–**8** (Figure 4a). (b) The crystallographically independent Ln^{3+} cations in **4**–**8** utilize eight-coordinated distorted trigonal dodecahedral geometries (Figure 4b), which are remarkably distinct from the 10-coordinated trigonal hexadecahedra in **1**–**2** and the nine-coordinated trigonal tetradecahedron in **3**. (c) In the 3-D

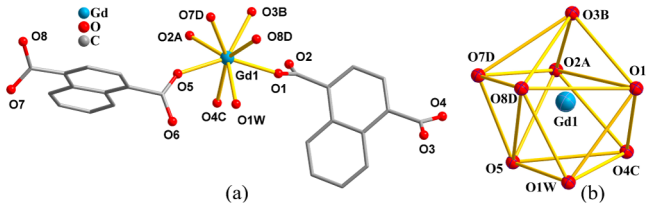

Figure 4. (a) Asymmetric molecular unit of **5**. The monoprotonated $[HBBI]^+$ cation is omitted for clarity. (b) Coordination polyhedron around the $Gd1^{3+}$ ion in **5**. Symmetric code: A: $1-x, 1-y, -z$; B: $x, 0.5-y, 0.5+z$; C: $1-x, -0.5+y, -0.5-z$; D: $2-x, 0.5+y, 0.5-z$..

extended frameworks of **4**–**8**, the NDC^{2-} ligands adopt the μ_3-η^1:η^1:η^1 and μ_4-η^1:η^1:η^1:η^1 bridging modes (Table 1). Specifically, neighboring dimeric molecular units are connected with each other by means of the μ_4-η^1:η^1:η^1:η^1-NDC^{2-} bridges, generating the 2-D sheets (Figure S4a in the Supporting Information), whereas adjacent 2-D sheets are further combined together by the μ_3-η^1:η^1:η^1-NDC^{2-} ligands to fabricate the 3-D frameworks with 1-D squarer channels filled by monoprotonated $[HBBI]^+$ cations (Figure S4b in the Supporting Information).

Optical Absorption Properties. To explore the optical properties of **1**–**8**, their optical diffuse reflectance spectra were measured using their powdered crystal samples to obtain the optical band gap (E_g). The band gap (E_g) was determined as the intersection point between the energy axis and the line extrapolated from the linear portion of the absorption edge in a plot of the Kubelka–Munk function F against energy E.[23] The Kubelka–Munk function, $F = (1-R)^2/2R$, was converted from the recorded diffuse reflectance data, where R is the reflectance of an infinitely thick layer at a given wavelength. The F versus E (eV) plots for **1**–**8** are shown in Figure S5 in the Supporting Information, from which the E_g can be evaluated at E_g = 3.22, 3.24, 3.29, 3.28, 3.34, 3.45, 3.19, and 3.26 eV for **1**, **2**, **3**, **4**, **5**, **6**, **7**, and **8**, respectively, suggesting that they possess the semiconductor characteristics.

Thermal Properties. To examine the thermal stability of **1**–**8**, TGA measurements have been performed on polycrystalline samples under air atmosphere with a heating rate of 10 °C/min in the temperature range 25–1000 °C (Figure S6 in the Supporting Information). Because the structures of **1**–**8** are very similar, only **1**, **3**, and **5** have been investigated. Complexes **1**, **3**, and **5** show simple thermal behavior and merely undergo three steps of weight loss. For **1**, the weight loss of 4.74% in the first step from 149 to 273 °C corresponds to the loss of one lattice water molecule and one coordination water molecule (calculated 4.88%). The second weight loss of 18.9% from 273 to 307 °C is assigned to the removal of one $HBBI^+$ ligand (calculated 18.3%) and the subsequent pyrolysis process from 307 to 1000 °C proceeded due to the decomposition of the network. The TGA curve of **3** shows three steps of weight loss. The first weight loss of 1.80% between 25 and 228 °C corresponds to the loss of one-half lattice water molecule and two coordination water molecules and one $HBBI^+$ ligand (calculated 1.83%). The second weight loss of 18.94% from 228 to 309 °C is attributable to the removal of two $[HBBI]^+$ ligands (calculated 18.35%). The third weight loss from 309 to 1000 °C is attributable to the decomposition of the network. For **5**, the dehydration of one coordinated water molecule occurred in the range 25–255 °C with a weight loss of 2.68% (calculated 2.44%). The weight loss of 18.62% (calculated 18.29%) from

dx.doi.org/10.1021/cg401825f | *Cryst. Growth Des.* 2014, 14, 1684–1694

255 to 305 °C is assigned to the removal of the $HBBI^+$ ligand and the subsequent pyrolysis process above 305 °C proceeded due to the decomposition of the network. The observed experimental values are in good agreement with the elemental analyses and the results of single-crystal X-ray structural analyses.

Magnetic Properties. Recently, Ln cations have been widely utilized in magnetic fields since the magnetic properties of Ln cations are largely influenced by spin−orbit couplings and in particular the magnetocrystalline anisotropy is generally large.[24] As we know, in contrast to the effects of the crystal field, the spin−orbital coupling generally plays a more important role in the magnetism of Ln complexes. This large spin−orbit coupling partly removes the degeneracy of the ^{2S+1}L group term of Ln cations, giving $^{2S+1}L_J$ states, which further split into Stark levels by crystal field perturbation.[25] Thus, the orbital component of the magnetic moment is much more important for Ln cations compared to transition-metal cations since crystal-field effects are smaller and spin−orbit coupling is larger for f electrons of Ln cations.[26] Therefore, except for the isotropic Gd^{III} cation having an $^8S_{7/2}$ single-ion ground state, not much is known about the nature and magnitude of the exchange interaction of Ln cations between themselves and the evolution of the magnetic properties along the Ln series.[27] One reason for this is that the orbital contribution occurs for the most Ln cations and the ligand field effect on the magnetic characteristics of the ions displays the spin−orbit coupling, which makes the quantitative interpretation of the magnetic data of their complexes very complicated.[27] At room temperature, all Stark sublevels of the $^{2S+1}L_J$ ground state or those of the low-lying first excited states for Sm^{III} and Eu^{III} cations are thermally populated. As the temperature drops, depopulation of these sublevels occurs and consequently the $\chi_{Ln}T$ decreases (χ_{Ln} is the magnetic susceptibility of the Ln cation). The temperature dependence of the χ_{Ln} deviates with respect to the Curie law.[27,28] Therefore, variable-temperature magnetic susceptibility measurements were performed with polycrystalline samples of **2**−**8** at an applied field of 1 kOe in the range 2−300 K.

For **2**, χ_M gradually increases from 0.011 emu mol^{-1} at 300 K to the maximum of 0.050 emu mol^{-1} at 2 K (Figure 5a). χ_MT is equal to 3.24 emu K mol^{-1} at 300 K, which is close to the expected value of 3.20 emu K mol^{-1} for two isolated Pr^{III} cations ($^3H_4$, $J = 4$, $g = 4/5$).[29] χ_MT declines gradually to 0.10 emu K mol^{-1} at 2 K. This decline is intimately related to the depopulation of the Stark levels upon cooling and/or the antiferromagnetic exchange interactions between two Pr^{III} cations mediated by bridging carboxylate groups. Fitting the data of χ_M^{-1} versus T between 300 and 80 K to the Curie−Weiss law gives $C = 3.73$ emu K mol^{-1} and $\theta = -44.13$ K (Figure 5b). The θ value is large, indicating the importance of ligand field effects in **2** and the presence of antiferromagnetic exchange interactions within Pr^{III} centers.[28,30]

As for **3**, χ_MT decreases from 0.22 emu K mol^{-1} at 300 K to 0.08 emu K mol^{-1} at 2 K upon cooling (Figure 5c). The curve of χ_M^{-1} versus T does not obey the Curie−Weiss law (Figure 5d) mainly because the Kramers doublets of higher energy are successively depopulated as the temperature decreases. The $^6H_{5/2}$ ground state for the free Sm^{III} cation in the crystal field is split into six states by spin−orbit coupling, and the spin−orbit coupling parameter is 1200 cm^{-1}. As a result, the crystal field effect and the possible thermal population of the high energy states should be considered for **3**.[31] The value of 0.08 emu K

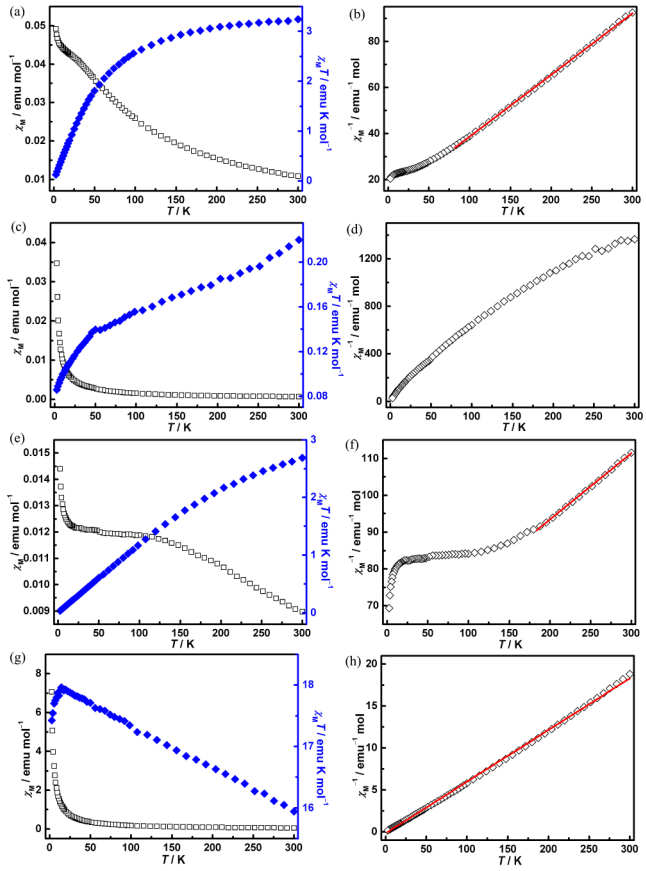

Figure 5. (a) Temperature dependence of magnetic susceptibility for **2** between 2 and 300 K. (b) Temperature evolution of the inverse magnetic susceptibility for **2** between 80 and 300 K. (c) Temperature dependence of magnetic susceptibility for **3** between 2 and 300 K. (d) Temperature evolution of the inverse magnetic susceptibility for **3** between 2 and 300 K. (e) Temperature dependence of magnetic susceptibility for **4** between 2 and 300 K. (f) Temperature evolution of the inverse magnetic susceptibility for **4** between 180 and 300 K. (g) Temperature dependence of magnetic susceptibility for **5** between 2 and 300 K. (h) Temperature evolution of the inverse magnetic susceptibility for **5** between 2 and 300 K. The red solid line was generated from the best fit by the Curie−Weiss expression.

mol^{-1} at 2 K is evidently smaller than that for two noninteractiong Sm^{III} cations (0.178 emu K mol^{-1}), revealing the occurrence of weak antiferromagnetic interactions within two Sm^{III} cations mediated by carboxylic oxygen atoms from NDC ligands as well as the spin−orbital coupling and the crystal field effect. This observation has been encountered in a dinuclear Sm^{III} complex $[Sm_2(4\text{-cba})_6(phen)_2(H_2O)_2]$[25] and a dinuclear Sm^{III} containing polyoxometalate $[\{(\alpha\text{-}PW_{11}O_{39})Sm(H_2O)(\eta^2,\mu\text{-}1,1)\text{-}CH_3COO\}_2]$.[31]

In the case of **4**, χ_M gradually increases from 0.001 emu mol^{-1} at 300 K to 0.012 emu mol^{-1} at 17 K, and then sharply increases to reach the maximum value of 0.015 emu mol^{-1} at 2 K (Figure 5e). At 300 K, χ_MT is equal to 2.69 emu K mol^{-1}, which roughly corresponds to the expected value (2.5 emu K mol^{-1}) for two isolated Eu^{III} cations.[25,32] As the temperature is lowered, χ_MT decreases continuously as a result of the progressive depopulation of the higher Stark levels for the Eu^{III} ions.[33] According to previous reports,[33,34] at 2 K the ground state of the Eu^{III} ion is $^7F_0$ and its χ_MT value is close to 0. However, the χ_MT value of **3** at 2.0 K of 0.03 emu K mol^{-1} suggests the presence of the antiferromagnetic couplings within

dx.doi.org/10.1021/cg401825f | Cryst. Growth Des. 2014, 14, 1684−1694

dinuclear Eu^{III} units. The curve of χ_M^{-1} versus T between 183 and 300 K follows the Curie–Weiss law with C = 5.56 emu K mol^{-1} and θ = −319.46 K (Figure 5f) because of the presence of thermally populated excited states.[32a,35] However, as the temperature decreases from 183 to 2 K, the relation of χ_M^{-1} versus T does not abide by the Curie–Weiss law. It is well-known that the ^7F ground term of the Eu^{III} cation is split by the spin–orbit coupling into seven states, ^7F_J, with J taking integer values from 0 to 6. Due to the small energy separation between the ground state and the first excited state, the first excited state may be thermally populated at room temperature and above.[25] Upon cooling, the depopulation of the higher Stark levels occurs, which also can result in the decrease of $\chi_M T$ and the magnetic behavior severely deviating from the Curie–Weiss law predicated by the free-ion approximation.[36] Furthermore, antiferromagnetic interactions within dinuclear Eu^{III} units can also make the curve of χ_M^{-1} versus T deviate from the Curie–Weiss law.

As for **5**, at 300 K, $\chi_M T$ is equal to 15.94 emu K mol^{-1}. This value corresponds to that expected value (15.74 emu K mol^{-1}) for two free Gd^{III} cations.[37] When the temperature is lowered, $\chi_M T$ gradually increases to the maximum of 17.98 emu K mol^{-1} at 18 K (Figure 5g). This behavior indicates weak ferromagnetic couplings within dinuclear Gd^{III} units. A sudden decrease of the $\chi_M T$ value below 18 K suggests the presence of intermolecular antiferromagnetic interactions. In the 2–300 K range, the magnetic susceptibility data could be described by a Curie–Weiss law with a Weiss constant θ = 3.23 K (Figure 5h), being consistent with the weak ferromagnetic coupling interactions.

For **6**, χ_M gradually increases from 0.079 emu mol^{-1} at 300 K to 0.975 emu mol^{-1} at 27 K and then exponentially increases to the maximum of 6.000 emu mol^{-1} at 2 K (Figure 6a). $\chi_M T$ at 300 K is 23.82 emu K mol^{-1}, which is equal to the theoretical value (23.64 emu K mol^{-1}) for two isolated Tb^{III} cations in the $^7F_6$ group state (J = 6, g = 3/2).[38] Upon cooling, $\chi_M T$ slowly increases to a maximum of 27.81 emu K mol^{-1} at 74 K, and then decreases on further cooling, reaching a minimum value of 11.97 emu K mol^{-1} at 2 K, indicating the ferromagnetic interactions between Tb^{III} centers. Moreover, the curve of χ_M^{-1} vs T in 300–145 K can obey the Curie–Weiss law with C = 21.31 emu K mol^{-1} and θ = 34.04 K (Figure 6b). The slow increase of $\chi_M T$ upon cooling and the positive θ value indicate that the weak ferromagnetic interactions between Tb^{III} centers dominate the magnetic behavior of **5**. In addition, as the temperature decreases from 145 to 2 K, the relation of χ_M^{-1} vs T somewhat does not conform to the Curie–Weiss law, being related to the occurrence of the intermolecular interactions.

With regard to **7**, the measured value of $\chi_M T$ at room temperature is 29.03 emu K mol^{-1} in agreement with the expected value of 28.34 emu K mol^{-1} for two uncorrelated Dy^{III} cations with a $^6H_{15/2}$ group state (J = 15/2, g = 4/3).[24b,39] As the temperature is lowered, $\chi_M T$ gradually increases to the maximum of 30.82 emu K mol^{-1} at about 96 K, and then decreases rapidly on further cooling, reaching the minimum value of 25.52 emu K mol^{-1} at 2 K, indicating weak ferromagnetic interactions between adjacent Dy^{III} cations. The maximum of $\chi_M T$ being only slightly higher than the value at room temperature implies that the ferromagnetic coupling is very weak. Furthermore, the curve of χ_M^{-1} vs T in the range 2–300 K can obey the Curie–Weiss law with C = 29.70 emu K mol^{-1} and θ = 0.64 K, which further confirms the weak ferromagnetic couplings between Dy^{III} cations.

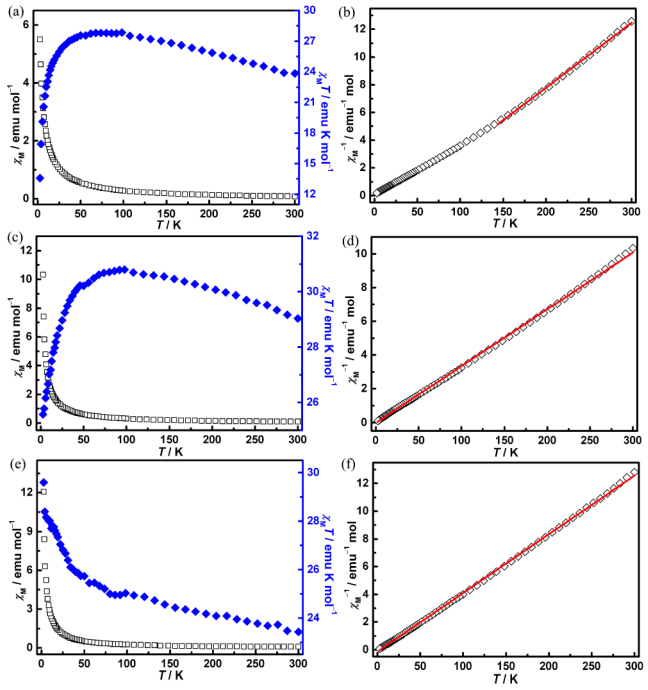

Figure 6. (a) Temperature dependence of magnetic susceptibility for **6** between 2 and 300 K. (b) Temperature evolution of the inverse magnetic susceptibility for **6** between 145 and 300 K. (c) Temperature dependence of magnetic susceptibility for **7** between 2 and 300 K. (d) Temperature evolution of the inverse magnetic susceptibility for **7** between 2 and 300 K. (e) Temperature dependence of magnetic susceptibility for **8** between 2 and 300 K. (f) Temperature evolution of the inverse magnetic susceptibility for **8** between 2 and 300 K. The red solid line was generated from the best fit by the Curie–Weiss expression.

For **8**, the χ_M value slowly increases from 0.078 emu mol^{-1} at 300 K to 0.65 emu mol^{-1} at 40 K and then exponentially reaches the maximum of 14.72 emu mol^{-1} at 2 K (Figure 6e). The value of $\chi_M T$ at 300 K of 23.42 emu K mol^{-1} is in line with the sum (22.96 emu K mol^{-1}) of the contribution attributable to two Er^{III} cations in the $^4I_{15/2}$ group state (J = 15/2, g = 6/5).[40] The $\chi_M T$ value increases to a maximum of 29.58 emu K mol^{-1} at about 2 K (Figure 6e). This behavior suggests the dominant ferromagnetic exchange interactions. The relationship of χ_M^{-1} versus T in 2–300 K obeys the Curie–Weiss law with C = 3.23 emu K mol^{-1} and θ = 23.60 K for **8**, which further consolidates the presence of the ferromagnetic exchange interactions (Figure 6f).

Photoluminescence Properties. Because Ln cation complexes are used as functional probes in biological systems and have range applications in lasers, sensors, electroluminescence displays, and light emitting diodes,[41a–c] study of the fluorescence of Ln complexes with aromatic ligands has attracted great interest. The low absorbance in rather narrow bands and weak luminescence direct excitation yields of free Ln cations, but their luminescence can be increased if the stable Ln complexes can be formed with suitable organic ligands, which can transfer their excitation energy to Ln centers (so-called "antenna effect"). To some degree, the emission intensity of Ln complexes strongly depends on the efficiency of the ligand absorption, ligand to metal charge transfer (LMCT), and Ln emission.[41d]

Here, the solid-state photoluminescence properties of **4** have been investigated at room temperature. Excitation of the as-

dx.doi.org/10.1021/cg401825f | Cryst. Growth Des. 2014, 14, 1684–1694

synthesized solid of **4** at 330 nm reveals five emission bands of the Eu^{III} ion (Figure 7), which are attributed to the $^5D_0 \rightarrow {}^7F_0$

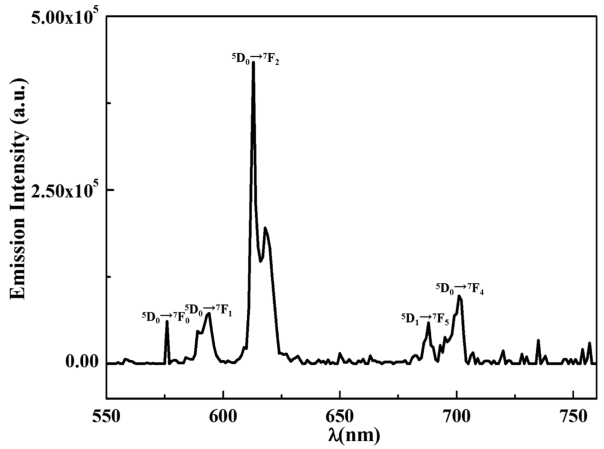

Figure 7. Solid-state emission spectra for **4** (Eu) (λ_{ex} = 330) at room temperature.

(576 nm), $^5D_0 \rightarrow {}^7F_1$ (588 nm), $^5D_0 \rightarrow {}^7F_2$ (613 nm), $^5D_1 \rightarrow {}^7F_5$ (688 nm), and $^5D_0 \rightarrow {}^7F_4$ (700 nm) transitions. These results are in good accordance with previous results.[41e,f] We also observed Stark splitting in some of these bands due to ligand field. The $^5D_0 \rightarrow {}^7F_1$ transitions are magnetic-dipolar transitions and insensitive to their local environments; however, the $^5D_0 \rightarrow {}^7F_2$ transitions are electric-dipolar transitions and sensitive to their local environments.[41g] In a site with an inversion, the $^5D_0 \rightarrow {}^7F_1$ transition is used as a reference to judge the environment asymmetry of the Ln because it is allowed by the magnetic dipole transition and its intensity is independent of the environment, whereas the hypersensitive transition strongly depends on it.[41g] In **4**, the $^5D_0 \rightarrow {}^7F_2$ transition at 613 nm is a hypersensitive electric dipole transition, and its intensity dominates over all other transitions. The much stronger intensity of this band indicates that the ligand field surrounding the Eu^{III} cation is highly polarizable[41h] and the lower symmetric coordination environment in **4**, which agrees well with the results of its single-crystal structure.

The determination of fluorescence lifetime is critical to the understanding of the "energy-handling" properties of excited states. Therefore, we measured the fluorescence lifetime of compound **4**, and the $5D_0$ emission decay curve was monitored within the $5D_0 \rightarrow 7F_2$ transition under the excitation wavelength (Figure 8). The decay curve cannot fit into the single-exponential function, but it can be well fit into a double-exponential function as $I = A + B_1 \exp(-t/\tau_1) + B_2 \exp(-t/\tau_2)$ (where τ_1 and τ_2 are the fast and slow components of the luminescent lifetimes and A, B_1, and B_2 are the fitting parameters), which is similar to the reported Eu^{III} coordination compound.[42] The lifetimes for $5D_0 \rightarrow 7F_2$ of the Eu^{III} ion were calculated to be τ_1 = 0.176 ms and τ_2 = 0.556 ms. Therefore, based on $\tau = (B_1\tau_1^2 + B_2\tau_2^2)/(B_1\tau_1 + B_2\tau_2)$,[43] the average lifetime of $5D_0 \rightarrow 7F_2$ for the Eu^{III} ion can be determined to be 0.534 ms (fitting parameters B_1 = 398.31 and B_2 = 3587.93). Although the system is quite complicated, preliminary results indicate that the excited state energy transfers from the organic ligands to the Eu^{III} cation through slow and faster energy from the ligands to the f orbital of rare-earth ions.

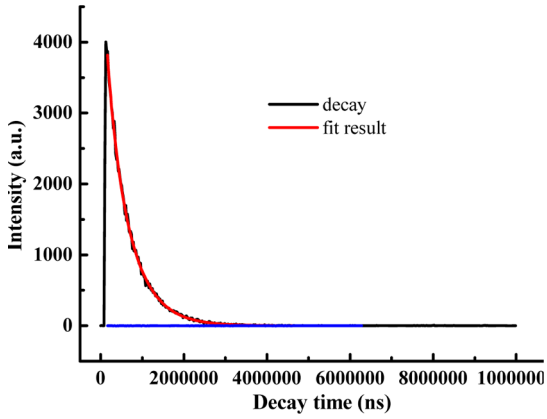

Figure 8. Decay curve of the $^5D_0 \rightarrow {}^7F_2$ excited stated of Eu^{III} in compound **4** under the single-exponential fitting condition.

CONCLUSIONS

In summary, we have successfully prepared eight Ln−NDC coordination polymers with BBI as templates {$[HBBI]_2[Ln(NDC)_2(H_2O)]_2 \cdot 2H_2O$ [Ln = La (**1**), Pr (**2**)], $[HBBI]_2[Sm(NDC)_2(H_2O)]_2 \cdot 1/2H_2O$ (**3**), and $[HBBI]_2[Ln(NDC)_2(H_2O)]_2$ [Ln = Eu (**4**), Gd (**5**), Tb (**6**), Dy (**7**), Er (**8**)]}, which have been structurally characterized. In particular, **1**−**8** display similar (8,8)-connected 3-D frameworks with different dinuclear Ln secondary building units due to the effect of Ln contraction and diverse coordination modes of NDC ligands. Furthermore, the magnetic properties of **2**−**8** have been measured. The thermal stabilities of **1**, **3**, and **5** have been investigated, which all indicate two steps of weight loss. More importantly, the luminescence properties of Eu (**4**) have been examined and its fluorescence lifetime has also been discussed in detail. In a word, the successful preparation of complexes **1**−**8** not only fertilizes the structural chemistry, but also opens the door to the possibility for the discovery of brighter luminescent Ln photonic materials.

ASSOCIATED CONTENT

Supporting Information

Selected bond lengths and bond angles of **1**−**8**; related structural figures of **2**, **3**, and **5**; hydrogen-bonding interactions in **2**, **3**, and **5**; optical absorption spectra for **1**−**8**; decay curve of **4**; crystal data in CIF format. This material is available free of charge via the Internet at http://pubs.acs.org. Crystallographic data for the structures reported here have been deposited at the Cambridge Crystallographic Data Centre (Deposition No. CCDC-956417 for **1**, 956418 for **2**, 956419 for **3**, 956420 for **4**, 956421 for **5**, 956422 for **6**, 956423 for **7**, and 956424 for **8**). These data can be obtained free of charge from the Cambridge Crystallographic Data Centre via www.ccdc.cam.ac.uk/data_request/cif.

AUTHOR INFORMATION

Corresponding Authors

*E-mail: ybluhm@163.com.
*E-mail: zhaojunwei@henu.edu.cn.

Notes

The authors declare no competing financial interest.

■ ACKNOWLEDGMENTS

We acknowledge financial support from the NSF of China (21161001), the NSF of Jiangxi Province (GJJ11724), and the Key Laboratory of Jiangxi University for Function of Materials Chemistry.

■ REFERENCES

(1) (a) Eddaoudi, M.; Moler, D. B.; Li, H. L.; Chen, B. L.; Reineke, T. M.; O'Keeffe, M.; Yaghi, O. M. *Acc. Chem. Res.* **2001**, *34*, 319−330. (b) Tan, Y. X.; He, Y. P.; Zhang, J. *Inorg. Chem.* **2012**, *51*, 9649−9654. (c) Kitagawa, S.; Kitaura, R.; Noro, S. *Angew. Chem., Int. Ed.* **2004**, *43*, 2334−2375. (d) Nguyen, T. N.; Wernsdorfer, W.; Abboud, K. A.; Christou, G. *J. Am. Chem. Soc.* **2011**, *133*, 20688−20691.

(2) (a) Zhuang, G. L.; Kong, X. J.; Long, L. S.; Huang, R. B.; Zheng, L. S. *CrystEngComm* **2010**, *12*, 2691−2694. (b) Lu, W. G.; Jiang, L.; Lu, T. B. *Cryst. Growth Des.* **2010**, *10*, 4310−4318.

(3) (a) Wu, M. F.; Wang, M. S.; Guo, S. P.; Zheng, F. K.; Chen, H. F.; Jiang, X. M.; Liu, G. N.; Guo, G. C.; Huang, J. S. *Cryst. Growth Des.* **2011**, *11*, 372−381.

(4) (a) Pan, L.; Sander, M. B.; Huang, X.; Li, J.; Smith, M.; Bittner, E.; Bockrath, B.; Johnson, J. K. *J. Am. Chem. Soc.* **2004**, *126*, 1308−1309. (b) Chen, P. K.; Qi, Y.; Che, Y. X.; Zheng, J. M. *CrystEngComm* **2010**, *12*, 720−724.

(5) (a) Li, Y. W.; Ma, H.; Chen, Y. Q.; He, K. H.; Li, Z. X.; Bu, X. H. *Cryst. Growth Des.* **2012**, *12*, 1064−1068. (b) Sun, D.; Luo, G. G.; Zhang, N.; Xu, Q. J.; Huang, R. B.; Zheng, L. S. *Polyhedron* **2010**, *29*, 1243−1250.

(6) (a) Maji, T. K.; Kaneko, W.; Ohba, M.; Kitagawa, S. *Chem. Commun.* **2005**, 4613−4615. (b) Yang, J.; Li, B.; Ma, J. F.; Liu, Y. Y.; Zhang, J. P. *Chem. Commun.* **2010**, *46*, 8383−8385.

(7) Eddaoudi, M.; Kim, J.; Rosi, N.; Vodak, D.; Wachter, J.; O'Keeffe, M.; Yaghi, O. M. *Science* **2002**, *295*, 469−472.

(8) Li, Y. W.; Ma, H.; Chen, Y. Q.; He, K. H.; Li, Z. X.; Bu, X. H. *Cryst. Growth Des.* **2012**, *12*, 189−196.

(9) (a) Zheng, X. J.; Li, L. C.; Gao, S.; Jin, L. P. *Polyhedron* **2004**, *23*, 1257−1262. (b) Chun, H.; Dybtsev, D. N.; Kim, H.; Kim, K. *Chem.—Eur. J.* **2005**, *11*, 3521−3529. (c) Vodak, D. T.; Braun, M. E.; Eddaoudi, J. M.; Yaghi, O. M. *Chem. Commun.* **2001**, 2534−2535. (d) Lu, J. Y.; Schauss, V. *Inorg. Chem. Commun.* **2002**, *5*, 1028−1030. (e) Lu, J. Y.; Schauss, V. *CrystEngComm* **2002**, *4*, 623−625. (f) Bickley, J. F.; Bonar-Law, R. P.; Femoni, C.; MacLean, E. J.; Steiner, A.; Teat, S. J. *J. Chem. Soc., Dalton Trans.* **2000**, 4025−4027. (g) Maji, T. K.; Ohba, M.; Kitagawa, S. *Inorg. Chem.* **2005**, *44*, 9225−9231. (h) Kanoo, P.; Gurunatha, K. L.; Maji, T. K. *J. Mater. Chem.* **2010**, *20*, 1322−1331. (i) Kanoo, P.; Maji, T. K. *Eur. J. Inorg. Chem.* **2010**, 3762−3769. (j) Wang, J. Y.; You, H. P. *Z. Anorg. Allg. Chem.* **2011**, *637*, 415−420. (k) Yang, J.; Che, G. B.; Liu, B.; Liu, Y. Y.; Ma, J. F. *Inorg. Chem. Commun.* **2010**, *13*, 112−115. (l) Furukawa, S.; Hirai, K.; Nakagawa, K.; Takashima, Y.; Matsuda, R.; Tsuruoka, T.; Kondo, M.; Haruki, R.; Tanaka, D.; Sakamoto, H.; Shimomura, S.; Sakata, O.; Kitagawa, S. *Angew. Chem., Int. Ed.* **2009**, *48*, 1766−1770. (m) Wang, X. L.; Chen, Y. Q.; Liu, G. C.; Lin, H. Y.; Zheng, W. Y.; Zhang, J. X. *J. Organomet. Chem.* **2009**, *694*, 2263−2269. (n) Furukawa, S.; Hirai, K.; Takashima, Y.; Nakagawa, K.; Kondo, M.; Tsuruoka, T.; Sakata, O.; Kitagawa, S. *Chem. Commun.* **2009**, 5097−5099. (o) Sun, D.; Luo, G. G.; Zhang, N.; Chen, J. H.; Huang, R. B.; Lin, L. R.; Zheng, L. S. *Polyhedron* **2009**, *28*, 2983−2988. (p) Jiang, X. J.; Guo, J. H.; Du, M.; Li, J. S. *Polyhedron* **2009**, *28*, 3759−3768. (q) Wang, X. L.; Chen, Y. Q.; Liu, G. C.; Lin, H. Y.; Zhang, J. X. *J. Solid State Chem.* **2009**, *182*, 2392−2401. (r) Fisher, M. G.; Gale, P. A.; Light, M. E.; Quesada, R. *CrystEngComm* **2008**, *10*, 1180−1190. (s) Comotti, A.; Bracco, S.; Sozzani, P.; Horike, S.; Matsuda, R.; Chen, J. X.; Takata, M.; Kubota, Y.; Kitagawa, S. *J. Am. Chem. Soc.* **2008**, *130*, 13664−13672. (t) Xiao, H. P.; Aghabeygi, S.; Zhang, W. B.; Cheng, Y. Q.; Chen, W. Y.; Wang, J.; Morsali, A. *J. Coord. Chem.* **2008**, *61*, 3679−3686. (u) Yang, J.; Ma, J. F.; Liu, Y. Y.; Ma, J. C.; Batten, S. R. *Cryst. Growth Des.* **2008**, *8*, 4383−4393. (v) Liu, G. C.; Chen, Y. Q.; Wang, X. L.; Chen, B. K.; Lin, H. Y. *J. Solid State Chem.* **2009**, *182*, 566−573. (w) Wu, R. F.; Zhang, T. L.; Zhang, J. G.; Qiao, X. J.; Yang, Li.; Guo, J. Y.; Wu, R. F. *Transition Met. Chem.* **2006**, *31*, 874−878. (x) Xu, Z. L.; He, Y.; Ma, S.; Wang, X. Y. *Transition Met. Chem.* **2011**, *36*, 585−591. (y) Yang, H.; Li, T. H.; Kang, Y.; Wang, F. *Inorg. Chem. Commun.* **2011**, *14*, 1695−1697. (z) Yan, L.; Li, C.; Zhu, D. S.; Xu, L. *J. Mol. Struct.* **2011**, *1002*, 172−178. (aa) Tan, B.; Xie, Z. L.; Huang, X. Y.; Xiao, X. R. *Inorg. Chem. Commun.* **2011**, *14*, 1001−1003. (ab) Liu, F. J.; Sun, D.; Hao, H. J.; Huang, R. B.; Zheng, L. S. *J. Mol. Struct.* **2012**, *1014*, 70−73. (ac) He, K. H.; Song, W. C.; Li, Y. W.; Chen, Y. Q.; Bu, X. H. *Cryst. Growth Des.* **2012**, *12*, 1064−1068.

(10) Zheng, X. J.; Jin, L. P.; Gao, S. *Inorg. Chem.* **2004**, *43*, 1600−1602.

(11) (a) Zheng, X. J.; Jin, L. P.; Gao, S.; Lu, S. Z. *New J. Chem.* **2005**, *29*, 798−804. (b) Zheng, X. J.; Jin, L. P.; Gao, S.; Lu, S. Z. *Inorg. Chem. Commun.* **2005**, *8*, 72−75.

(12) Yang, J.; Yue, Q.; Li, G. D.; Cao, J. J.; Li, G. H.; Chen, J. S. *Inorg. Chem.* **2006**, *45*, 2857−2865.

(13) Zhang, J.; Bu, J. T.; Chen, S. M.; Wu, T.; Zheng, S. T.; Chen, Y. G.; Nieto, R. A.; Feng, P. Y.; Bu, X. H. *Angew. Chem., Int. Ed.* **2010**, *49*, 8876−8879.

(14) (a) Yang, J.; Ma, J. F.; Liu, Y. Y.; Ma, J. C.; Batten, S. R. *Cryst. Growth Des.* **2009**, *9*, 1894−1911. (b) Satha, P.; Illa, G.; Purohit, C. S. *Cryst. Growth Des.* **2013**, *13*, 2636−2641. (c) Lin, J. D.; Wang, S. H.; Cai, L. Z.; Zheng, F. K.; Guo, G. C.; Huang, J. S. *Dalton Trans.* **2013**, *42*, 6429−6439. (d) Li, L.; Yue, J. M.; Qiao, Y. Z.; Niu, Y. Y.; Hou, H. W. *CrystEngComm* **2013**, *15*, 3835−3842.

(15) Wang, X. Y.; Wang, Z. M.; Gao, S. *Chem. Commun.* **2008**, 281−294.

(16) (a) Yang, J.; Ma, J. F.; Batten, S. R.; Su, Z. M. *Chem. Commun.* **2008**, 2233−2235. (b) Yang, J.; Ma, J. F.; Liu, Y. Y.; Ma, J. C.; Batten, S. R. *Cryst. Growth Des.* **2008**, *8*, 4383−4393.

(17) *CrystalClear*, version 1.35; *Software User's Guide for the Rigaku R-Axis, and Mercury and Jupiter CCD Automated X-ray Imaging System*; Rigaku Molecular Structure Corp.: Tokyo, 2002.

(18) *SHELXTL Reference Manual*, version 5; Siemens Energy & Automation Inc.: Madison, WI, 1994.

(19) Zhang, D.; Lu, Y.; Chen, L.; Cai, H.; Zhu, D. R.; Xu, Y. *CrystEngComm* **2012**, *14*, 6627−6638.

(20) Xu, J.; Cheng, J.; Su, W.; Hong, M. *Cryst. Growth Des.* **2011**, *11*, 2294−2301.

(21) (a) Ockwig, N. W.; Delgado-Fridrichs, O.; O'Keeffe, M.; Yaghi, O. M. *Acc. Chem. Res.* **2005**, *38*, 176−182. (b) Hill, R. J.; Long, D. L.; Champness, N. R.; Hubberstey, P.; Schröder, M. *Acc. Chem. Res.* **2005**, *38*, 337−350.

(22) (a) Abrahams, B. F.; Haywood, M. G.; Robson, R. *J. Am. Chem. Soc.* **2005**, *127*, 816−817. (b) Du, M.; Zhang, Z.-H.; Tang, L.-F.; Wang, X.-G.; Zhao, X.-J.; Batten, S. R. *Chem.—Eur. J.* **2007**, *13*, 2578−2586. (c) Liu, Y.; Xu, X.; Zheng, T.; Cui, Y. *Angew. Chem., Int. Ed.* **2008**, *47*, 4538−4541.

(23) (a) Wesley, W. M.; Harry, W. G. H *Reflectance Spectroscopy*; Wiley: New York, 1966; pp 104−169. (b) Pankove, J. I. *Optical Processes in Semiconductors*; Prentice Hall: Englewood Cliffs, NJ, 1997; pp 34−86.

(24) (a) Benelli, C.; Gatteschi, D. *Chem. Rev.* **2002**, *102*, 2369−2387. (b) Sun, Y. Q.; Zhang, J.; Chen, Y. M.; Yang, G. Y. *Angew. Chem., Int. Ed.* **2005**, *44*, 5814−5817. (c) Zhang, Z. H.; Song, Y.; Okamura, T. A.; Hasegawa, Y.; Sun, W. Y.; Ueyama, N. *Inorg. Chem.* **2006**, *45*, 2896−2902. (d) Zhang, S.; Wang, Y.; Zhao, J.; Ma, P.; Wang, J.; Niu, J. *Dalton Trans.* **2012**, *41*, 3764−3772.

(25) Li, Y.; Zheng, F. K.; Liu, X.; Zou, W. Q.; Guo, G. C.; Lu, C. Z.; Huang, J. S. *Inorg. Chem.* **2006**, *45*, 6308−6316.

(26) Kahn, O. *Adv. Inorg. Chem.* **1995**, *43*, 179−259.

(27) (a) Kahn, M. L.; Sutter, J.; Golhen, S.; Guionneau, P.; Ouahab, L.; Kahn, O.; Chasseau, D. *J. Am. Chem. Soc.* **2000**, *122*, 3413−3421. (b) Zhao, J. W.; Luo, J.; Chen, L. J.; Yuan, J.; Li, H. Y.; Ma, P. T.; Wang, J. P.; Niu, J. Y. *CrystEngComm* **2012**, *14*, 7981−7993.

(28) Costes, J. P.; Dahan, F.; Dupuis, A.; Laurent, J. P. *Chem.—Eur. J.* **1998**, *4*, 1616−1620.

(29) Peristeraki, T.; Samios, M.; Siczek, M.; Lis, T.; Milios, C. J. *Inorg. Chem.* **2011**, *50*, 5175−5185.

(30) Tang, J. K.; Li, Y. Z.; Wang, Q. L.; Gao, E. Q.; Liao, D. Z.; Jiang, Z. H.; Yan, S. P.; Cheng, P.; Wang, L. F.; Wang, G. L. *Inorg. Chem.* **2002**, *41*, 2188−2192.
(31) Niu, J. Y.; Wang, K. H.; Chen, H. N.; Zhao, J. W.; Ma, P. T.; Wang, J. P.; Li, M. X.; Bai, Y.; Dang, D. B. *Cryst. Growth Des.* **2009**, *9*, 4362−4372.
(32) (a) Wan, Y. H.; Zhang, L. P.; Jin, L. P.; Gao, S.; Lu, S. Z. *Inorg. Chem.* **2003**, *42*, 4985−4994. (b) Zhao, J. W.; Shi, D. Y.; Chen, L. J.; Li, Y. Z.; Ma, P. T.; Wang, J. P.; Niu, J. Y. *Dalton Trans.* **2012**, *41*, 10740−10751.
(33) Zhang, Z. H.; Okamura, T.; Hasegawa, Y.; Kawaguchi, H.; Kong, L. Y.; Sun, W. Y.; Ueyama, N. *Inorg. Chem.* **2005**, *44*, 6219−6227.
(34) Costes, J. P.; Dahan, F.; Dupuis, A.; Laurent, J. P. *Chem.—Eur. J.* **1998**, *4*, 1616−1620.
(35) Zheng, X. J.; Sun, C. Y.; Lu, S. Z.; Liao, F. H.; Gao, S.; Jin, L. P. *Eur. J. Inorg. Chem.* **2004**, 3262−3268.
(36) He, F.; Tong, M. L.; Yu, X. L.; Chen, X. M. *Inorg. Chem.* **2005**, *44*, 559−565.
(37) Hernández-Molina, M.; Ruiz-Pérez, C.; López, T.; Lloret, F.; Julve, M. *Inorg. Chem.* **2003**, *42*, 5456−5458.
(38) Li, Z. Y.; Zhu, G. S.; Guo, X. D.; Zhao, X. J.; Jin, Z.; Qiu, S. L. *Inorg. Chem.* **2007**, *46*, 5174−5178.
(39) Caneschi, A.; Dei, A.; Gatteschi, D.; Poussereau, S.; Sorace, L. *Dalton Trans.* **2004**, 1048−1055.
(40) (a) Kahn, M. L.; Ballou, R.; Porcher, P.; Kahn, O.; Sutter, J. P. *Chem.—Eur. J.* **2002**, *8*, 525−531. (b) Feng, X.; Zhao, J. S.; Liu, B.; Wang, L. Y.; Ng, S.; Zhang, G.; Wang, J. G.; Shi, X. G.; Liu, Y. Y. *Cryst. Growth. Des.* **2010**, *10*, 1399−1408. (c) Zhang, Z. H.; Song, Y.; Okamura, T. A.; Hasegawa, Y.; Sun, W. Y.; Uwyama, N. *Inorg. Chem.* **2006**, *45*, 2896−2902.
(41) (a) Mishra, V.; Mishra, H. *J. Phys. Chem. B* **2008**, *112*, 4213−4222. (b) de Sá, G. F.; Malta, O. L.; Donega, C. D.; Simas, A. M.; Longo, R. L.; Santa-Cruz, P. A.; da Silva, E. F. *Coord. Chem. Rev.* **2000**, *196*, 165−195. (c) Yanagida, S.; Hasegawa, Y.; Murakoshi, K.; Wada, Y.; Nakashima, N.; Yamanaka, T. *Coord. Chem. Rev.* **1998**, *171*, 461−480. (d) Luo, Y. H.; Yan, Q.; Wu, S.; Wu, W. X.; Zhang, Q. J. *J. Photochem. Photobiol., A* **2007**, *191*, 91−96. (e) Xia, J.; Zhao, B.; Wang, H. S.; Shi, W.; Ma, Y.; Song, H. B.; Cheng, P.; Liao, D. Z.; Yan, S. P. *Inorg. Chem.* **2007**, *46*, 3450−3458. (f) Singh, A. K.; Singh, S. K.; Mishra, H.; Prakash, R.; Rai, S. B. *J. Phys. Chem. B* **2004**, *114*, 13042−13051. (g) Xu, Q. H.; Li, L. S.; Liu, X. S.; Xu, R. R. *Chem. Mater.* **2002**, *14*, 549−555. (h) Liang, H.; Chen, B.; Xu, J.; Su, W.; Guo, F.; Guo, B.; Zhang, Q.; Zheng, Z.; Ming, H. *Mater. Lett.* **2005**, *59*, 4030−4033.
(42) Liu, Q. Y.; Wang, W. F.; Wang, Y. L.; Shan, Z. M.; Wang, M. S.; Tang, J. *Inorg. Chem.* **2012**, *51*, 2381−2392.
(43) Fujii, T.; Kodaira, K.; Kawauchi, O.; Tanaka, N.; Yamashita, H.; Anpo, M. *J. Phys. Chem. B* **1997**, *101*, 10631.